The Astrophysical Journal, 923:208 (12pp), 2021 December 20 https://doi.org/10.3847/1538-4357/ac23cf

Lepton-driven Nonresonant Streaming Instability

Siddhartha Gupta[1], Damiano Caprioli[1,2], and Colby C. Haggerty[3]
[1] Department of Astronomy and Astrophysics, University of Chicago, IL 60637, USA; gsiddhartha@uchicago.edu
[2] Enrico Fermi Institute, University of Chicago, IL 60637, USA
[3] Institute for Astronomy, University of Hawaii, Honolulu, HI, USA
Received 2021 June 10; revised 2021 September 1; accepted 2021 September 2; published 2021 December 22

Abstract

A strong super-Alfvénic drift of energetic particles (or cosmic rays) in a magnetized plasma can amplify the magnetic field significantly through nonresonant streaming instability (NRSI). While the traditional analysis is done for an ion current, here we use kinetic particle-in-cell simulations to study how the NRSI behaves when it is driven by electrons or by a mixture of electrons and positrons. In particular, we characterize the growth rate, spectrum, and helicity of the unstable modes, as well the level of the magnetic field at saturation. Our results are potentially relevant for several space/astrophysical environments (e.g., electron strahl in the solar wind, at oblique nonrelativistic shocks, around pulsar wind nebulae), and also in laboratory experiments.

Unified Astronomy Thesaurus concepts: Plasma astrophysics (1261); Plasma physics (2089); Cosmic rays (329); Magnetic fields (994); Shocks (2086)

1. Introduction

Interactions between energetic charged particles and a thermal background plasma generate a wide variety of instabilities, ultimately fueled by the anisotropy of the nonthermal particles relative to the background plasma. They are generally known as streaming instabilities (for reviews see, e.g., Bykov et al. 2013; Zweibel 2013) and may produce large amplitude modes over a broad range of scales, from the ion skin depth (∼100 km in the interstellar medium) to the parsec scale of the gyroradius of the highest energy Galactic cosmic rays (CRs). These instabilities are crucial for the generation of magnetic fields, the acceleration and propagation of nonthermal particles, and for the heating of space and astrophysical plasmas. Finally, modern laser facilities are unlocking the possibility of also studying streaming instabilities in the laboratory, even in the collisionless regime (e.g., Jao et al. 2019).

In the context of the interactions between CRs and a thermal background plasma, there are two main regimes of interest: the resonant and nonresonant streaming instabilities (hereafter RSI and NRSI, respectively), with the latter dominant for strong CR currents (Bell 2004; Amato & Blasi 2009).

The NRSI is characterized by the fastest-growing mode with wavelength $\lambda_{\rm fast} \approx c\, B_0/J_{\rm cr}$, where $J_{\rm cr}$ is the CR current density in the direction of the mean magnetic field B_0 and c is the speed of light. The instability is dubbed nonresonant because the wavelength of the fastest-growing modes is much shorter than the CR gyroradius (R_L), i.e., $\lambda \ll R_L$ and the unstable modes have right-handed (RH) circular polarization (so the fastest-growing mode of magnetic field does not rotate in the same direction as current-carrying CR ions).

While a magnetized plasma is typically considered for the NRSI, it is worth mentioning that this instability can be triggered even in the absence of an initial magnetic field due to the results of other interactions such as the Weibel instability (Weibel 1959), which can provide the seed magnetic field (see, e.g., Peterson et al. 2021).

Although the idea was already present in the derivations of Achterberg (1983) and Winske & Leroy (1984), nonresonant modes were recognized as crucial for CR scattering by Bell (2004), after it has been shown that CR-driven instabilities may strongly amplify the initial magnetic field to nonlinear values of $\delta B/B_0 \gg 1$ (Bell & Lucek 2001).

1.1. Lepton-driven NRSI

The NRSI (also called nonresonant hybrid, or simply Bell, instability) has been studied extensively with analytical, MHD, and kinetic approaches (e.g., Niemiec et al. 2008; Zirakashvili & Ptuskin 2008; Amato & Blasi 2009; Bret 2009; Riquelme & Spitkovsky 2009; Gargaté et al. 2010; Reville & Bell 2013; Matthews et al. 2017; Haggerty et al. 2019; Weidl et al. 2019; Zacharegkas et al. 2019; Marret et al. 2021), always under the assumption that the current is carried by protons. The motivation for this choice is that the electron/ion ratio in CR fluxes at Earth is rather small, $\lesssim 10^{-2}$–10^{-3}, as it is in sources such as supernova remnants (e.g., Berezhko & Völk 2004; Morlino & Caprioli 2012).

Nevertheless, there are several instances in which a strong current driven by nonthermal leptons may arise. For instance, in quasi-perpendicular shocks (where the pre-shock magnetic field makes an angle $\gtrsim 60^\circ$ with the shock normal) the injection of thermal ions is suppressed (Caprioli et al. 2015) but electrons can still be injected and undergo shock acceleration (e.g., Guo et al. 2014a, 2014b; Bohdan et al. 2019; Xu et al. 2020). Another environment where strong lepton currents can be generated are pulsar wind nebulae (PWNe), which are leptonic sources that can accelerate electrons and positrons up to petaelectronvolt energies. Recently, γ-ray halos have been discovered around nearby PWNe (Abeysekara et al. 2017; Schroer et al. 2021), attesting to the fact that escaping leptons can strongly modify the interstellar magnetic fields, leading to particle self-confinement. Note that, even if the seeds for PWN relativistic particles are likely magnetospheric pairs, the highest energy leptons are found to be of a given sign, depending on the relative orientation of the pulsar magnetic and rotation axes (e.g., Cerutti et al. 2015; Philippov 2017; Philippov & Spitkovsky 2018).

There are also plasma systems closer to Earth where nonthermal electrons are important, such as the strahl in the solar wind or planetary bow shocks (e.g., Masters et al. 2013; Wilson et al. 2016; Masters et al. 2017; Malaspina et al. 2020). Within 30 $R_\odot$ of the Sun, the momentum flux of the electron

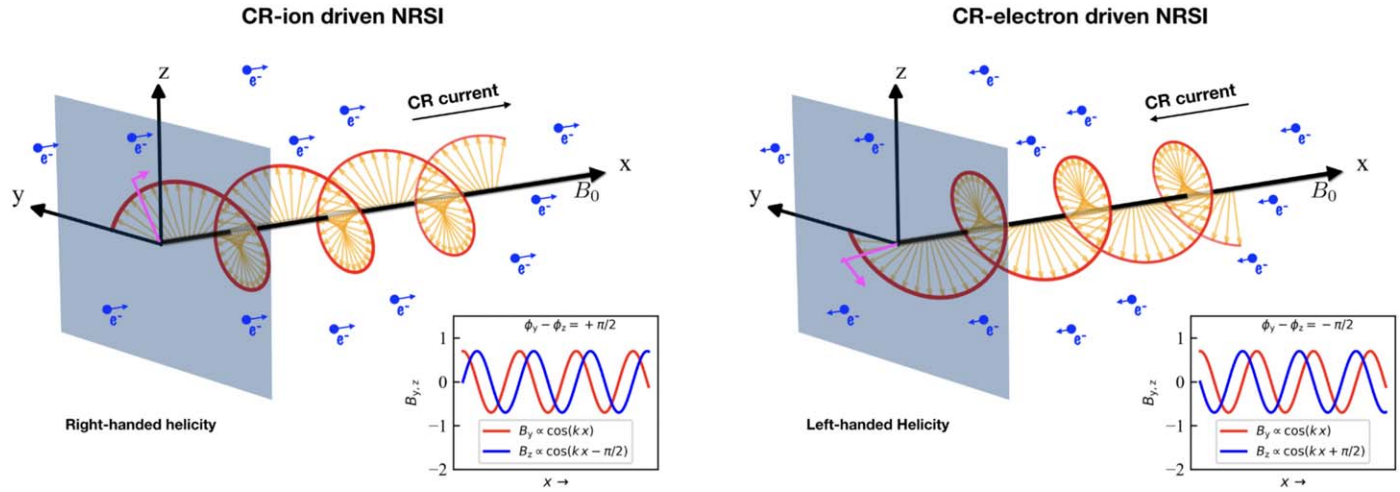

Figure 1. Schematic diagram showing the structure of the amplified magnetic field for CR-I (left) and CR-E (right). CRs are drifting parallel to an initial magnetic field $B_0\hat{x}$, which produces a current denoted by a black arrow. Blue circles represent the plasma electrons, where the arrows indicate the drift velocity (in the plasma frame) that compensates the CR current. This system is unstable and produces transverse (y, z directions) waves. The expected phase difference between the transverse (growing) components of the magnetic field ($B_{y,z}$) is shown in the box. Considering the transverse components $B_{y,z} \propto \exp[j(kx + \phi_{y,z})]$, for a given k, if $\Delta\phi = \phi_y - \phi_z > 0$ then the transverse B field, $B_y\hat{\boldsymbol{y}} + B_z\hat{\boldsymbol{z}}$, rotates clockwise as one moves along the positive x-axis. We refer this as an RH mode and opposite to it as a left-handed (LH) mode. The figure shows that in the CR-I (CR-E) case, the waves are RH (LH) with respect to the direction of the initial magnetic field (B_0).

strahl is within an order of magnitude of reaching the nonresonant threshold that will be discussed in this work (Kasper et al. 2019; Halekas et al. 2020, as determined from recent in situ measurements reported from the first few perihelion passes of Parker Solar Probe). The nearest to the instability threshold suggests that the electron-driven NRSI may be occurring closer to the Sun where the momentum flux of nonthermal electrons is expected to be larger, and that this instability can be responsible for the scattering of the strahl.

Electron-driven NRSI may finally be of interest for laboratory plasma experiments (Bret et al. 2010). With very powerful lasers, it is possible to reproduce the collisionless conditions typical of astrophysical systems. While experiments have not been able to recreate the condition to drive the NRSI with ions, to our knowledge, a few works have attempted to do so with electrons (e.g., Jao et al. 2019). Therefore, it is important to put forward a theory of lepton-driven NRSI and validate it via kinetic simulations, which is the scope of this work.

Bell's derivation of the NRSI (Bell 2004) highlights how, as long as the CRs are infinitely rigid, the maximally unstable mode and its associated growth rate depend on the compensating current induced in the background plasma. At the first order in the small parameter $n_{\rm cr}/n$, i.e., the ratio in CR to thermal number density, the NRSI growth rate is independent of the composition of the CR distribution and only depends on the net induced return current (also see Amato & Blasi 2009; Weidl et al. 2019); however, it is nontrivial that the return current, which is supported by the light thermal electrons, behaves the same for negatively charged CRs, or for CR distributions with both positive and negative charges.

In this work, we derive the NRSI for CRs with arbitrary mass and charge and in particular to address the following questions:

1. What are the necessary conditions for having lepton-driven NRSI?
2. What are the properties of the fastest-growing modes (polarization, wavelength, and growth rate)?
3. Can CRs with a mixed (e.g., electrons and positrons) composition produce NRSI?
4. Is the saturation of the amplified magnetic field the same as in the ion-driven case?

We begin by outlining the analytical linear theory for the NRSI driven by CRs of arbitrary mass and charge in Section 2. In Section 3, we introduce self-consistent particle-in-cell (PIC) simulations used to test both ion- and electron-driven NRSI (henceforth, CR-I and CR-E), which are compared and discussed in Section 4. The implications of this study for different plasma backgrounds (e.g., electron-positron) and mixed compositions of CRs are also discussed in Section 4. We conclude in Section 5.

2. Linear Theory

The theory of NRSI driven by energetic CRs propagating along magnetic field lines has been studied in both the fluid and kinetic limits (Bell 2004; Amato & Blasi 2009; Riquelme & Spitkovsky 2009; Zweibel & Everett 2010); here, we present a simple derivation that explicitly assumes that resonant interactions between CRs and growing waves are negligible (see Section 2.3), for an arbitrary mass and charge of CRs.

The bulk motion of CRs produces a strong current in the plasma, which needs to be compensated by the drift of thermal background electrons. Such a drift velocity can be found by balancing the currents of the CRs and the background, i.e.,

$$\boldsymbol{v}_e = s_{\rm cr}\frac{n_{\rm cr}}{n_e}\boldsymbol{v}_d. \tag{1}$$

Here, $\boldsymbol{v}_d$ is the CR drift velocity with respect to the thermal ions (the analysis is done in the ion rest frame), and $n_{\rm cr}$ and n_e are the number density of CRs and background electrons, respectively. We pose $\boldsymbol{v}_d = v_d\hat{\boldsymbol{x}}$, so that the return current electrons drift along the positive/negative x-axis, depending on the sign of the charge of the CRs ($s_{\rm cr} = \pm 1$), as sketched in Figure 1. Quasi-neutrality requires that the number density of ions, electrons, and CRs must balance, i.e., $n_e = n_i + s_{\rm cr}\, n_{\rm cr}$. In typical astrophysical applications, the CR number density is

much smaller than the density of the background plasma ($n_{cr} \ll n_i \approx n_e \equiv n_0$), so that $v_e \ll v_d$.

The motion of any particle in the species α is given by the Lorentz force:

$$m_\alpha \frac{d\boldsymbol{v}_\alpha}{dt} = q_\alpha \left[\boldsymbol{E} + \frac{\boldsymbol{v}_\alpha}{c} \times \boldsymbol{B} \right], \tag{2}$$

where $\boldsymbol{v}_\alpha$ is the velocity of a particle of mass m_α and charge q_α (representing ions, electrons, hereafter $\alpha = i, e$), $\boldsymbol{E}$ and $\boldsymbol{B}$ are the electric and magnetic field. We consider a system with no initial electric field ($\boldsymbol{E} = 0$) and a uniform magnetic field $\boldsymbol{B} = B_0 \hat{\boldsymbol{x}}$. Assuming that the background population is sufficiently cold, so that initially $\boldsymbol{v}_i \approx 0$ and $\boldsymbol{v}_e$ is given by Equation (1), we can linearize Equation (2) along with Maxwell equations (for details see Appendix A) by considering small plane-wave perturbations $\propto \exp[j(kx - \omega t)]$ (Krall & Trivelpiece 1973; Achterberg 1983; Choudhuri 1998), where k and ω are the usual (parallel) wavenumber and the angular frequency of the plasma modes. With an additional assumption that $|\omega| \ll \omega_{ci}$, i.e., that both the instability growth rate (the imaginary part of ω) and the phase speed (the real part of ω) of the modes are much smaller than the ion cyclotron frequency, ω_{ci}, we obtain the following dispersion relations for LH and RH modes:[4]

$$\omega_{R,L} \approx \pm s_{cr} \frac{1}{2} \frac{n_{cr}}{n_e} \omega_{ci} + v_{A0}\, k \times \left[1 \mp s_{cr} \frac{k_u}{k} \right]^{1/2}. \tag{3}$$

Here, $v_{A0} \equiv B_0/(4\pi\, m_i\, n_0)^{1/2}$ is the Alfvén speed and we have introduced the critical wavenumber

$$k_u \equiv \frac{\omega_{ci}\, |v_e|}{v_{A0}^2} = \frac{\omega_{ci}}{v_{A0}} \frac{n_{cr}}{n_e} \frac{v_d}{v_{A0}}. \tag{4}$$

This makes it evident that, for a given CR charge s_{cr}, one branch of modes becomes unstable for $k < k_u$ and for small k, the growth rate is suppressed $\propto k^{1/2}$. The phase difference between transverse components of the perturbed magnetic field is (see Equations (A5) and (A9)):

$$\Delta\phi \equiv \phi_y - \phi_z = \pm \frac{\pi}{2}. \tag{5}$$

Therefore, the helicity of the transverse magnetic field is determined by the upper/lower sign of the dispersion relation (Equation (3)), with the positive and negative sign corresponding to the RH and LH modes, respectively. Figure 1 sketches the expected helicity of the resulting modes for the CR-I and CR-E driven cases and Figure 2 summarizes the different regimes of Equation (3) as a function of k/k_u.

2.1. Regime I: $k > k_u$

This regime (gray-shaded region in Figure 2) corresponds to oscillatory modes with wavelength smaller than the ion inertial length c/ω_{pi}, where ω_{pi} is the ion plasma frequency.

2.2. Regime II: $k < k_u$

In this regime (white region in Figure 2), ω has both real and imaginary parts. Depending on the CR charge, either RH or LH modes will be amplified: for CR-I/CR-E (i.e., $s_{cr} = +1/-1$) waves grow when the upper/lower sign of Equation (3) is

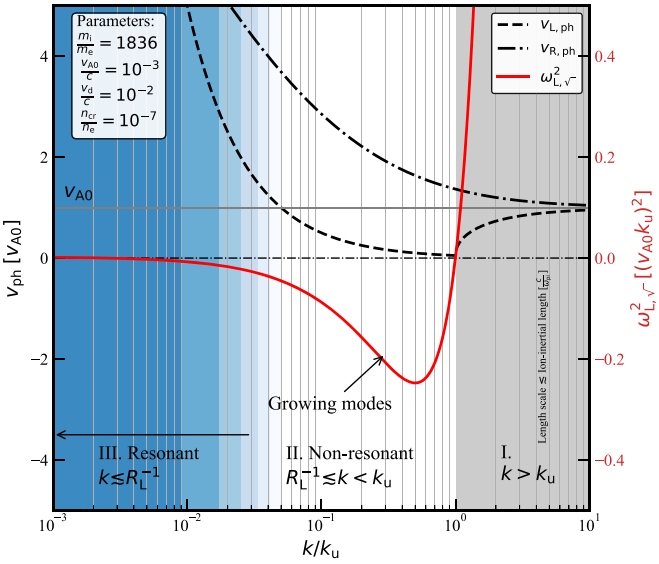

Figure 2. Phase speed and the growing/damping part of the angular frequency (the second term in the right side of Equation (3): $\omega^2_{L,\sqrt{-}}$) as a function of k for CR-I (using $s_{cr} = -1$ in Equation (3)). The figure shows $\omega^2_{L,\sqrt{-}} < 0$ when $\kappa < k_u$ (Regime II). In this regime, although the phase speed of the LH modes (dashed curve) are smaller than both the CR drift velocity ($v_d = 10\, v_{A0}$) and the Alfvén speed (in the limit $k \to k_u$), the waves gain energy. This is the nonresonant mode (Bell 2004).

chosen, corresponding to the RH and LH modes, respectively. While Equation (3) accurately captures the growth rate of the most unstable branch in the limit $v_d \gg v_A$, the present derivation does not extend to the weak-current limit, in which the resonant modes grow with much smaller rate; the RSI solution appear only in a kinetic calculation done in the proper wave frame (Zweibel 1979; Achterberg 1983; Bell 2004; Amato & Blasi 2009).

From Equation (3) we also see that the phase speed of the growing modes (RH/LH in the CR-I/CR-E case) is

$$v_{ph} \approx \frac{1}{2} \frac{n_{cr}}{n_e} \frac{\omega_{ci}}{k} = \frac{1}{2} \frac{v_{A0}^2}{v_d} \frac{k_u}{k}, \tag{6}$$

consistent with Riquelme & Spitkovsky (2009). Since we have taken $v_{A0} \ll v_d$, the phase velocity (dashed curve in Figure 2) and group velocity are much smaller than the drift velocity of plasma electrons, i.e., nonresonant modes are almost stationary in the plasma frame as $k \to k_u$. Whereas the phase speed of the other branch (dashed–dotted curve in Figure 2) is typically larger than v_{A0}; for a smaller k/k_u, close to resonant scales, v_{ph} of both LH and RH branches is larger than v_{A0}. This can be important in determining the speed of the CR scattering centers in shock environments, where they contribute to shaping the shock dynamics and the CR spectra (e.g., Caprioli et al. 2020; Haggerty & Caprioli 2020).

It is straightforward to show that (Appendix A), irrespective of the composition of CRs, the fastest-growing mode is at $k_{fast} = k_u/2$:

$$k_{fast} \equiv \frac{1}{2} \frac{v_e}{v_{A0}} \frac{1}{d_i} = \frac{1}{2} \frac{n_{cr}}{n_e} \frac{v_d}{v_{A0}} \frac{1}{d_i}, \tag{7}$$

[4] The convention is illustrated in Figure 1.

where $d_i = c/\omega_{\rm pi} = v_{A0}/\omega_{\rm ci}$ is the ion skin depth, and the corresponding growth rate is

$$\gamma_{\rm fast} \equiv k_{\rm fast}\, v_{A0} = \frac{1}{2}\frac{n_{\rm cr}}{n_e}\frac{v_d}{v_{A0}}\,\omega_{\rm ci}. \quad (8)$$

2.3. Regime III: $k \ll k_u$

The above derivation is oblivious to any resonant interaction between CRs and growing modes, and hence holds as long as $kR_L \gg 1$, where $R_L = p_{\rm cr}c/eB_0$ is the gyroradius of a CR with momentum $p_{\rm cr}$; such an assumption must break for sufficiently small k (blue-shaded region III in Figure 2). Fully kinetic calculations show that in this regime the NRSI becomes comparable to, or even less important than, the RSI (Amato & Blasi 2009; Haggerty et al. 2019). Although the exact transition from NRSI to RSI depends on the shape of the CR distribution function, in general the NRSI dominates when $k_{\rm fast}R_L \gg 1$, which corresponds to:

$$\xi \equiv \frac{n_{\rm cr}}{n_0}\frac{p_{\rm cr}}{m_i}\frac{v_d}{v_{A0}^2} \equiv \frac{1}{2}\frac{P_{\rm cr}}{P_{\rm B0}} \gg 1, \quad (9)$$

where $P_{\rm B0}$ is the magnetic pressure and $P_{\rm cr}$ is the CR momentum flux (anisotropic pressure) along x. In general, the NRSI can be triggered if a charged species has an anisotropic pressure that exceeds the magnetic one (see, e.g., Figure 9 in Appendix B); to some extent, it could be thought of as a firehose instability driven by charged particles (e.g., Shapiro et al. 1998, and references therein).

Note that ξ in Equation (9) depends on the momentum of CR particles divided by the *ion* mass, which means that for relativistic electrons to satisfy the condition $\xi \gg 1$, their Lorentz factor γ_e has to be a factor of $m_i/m_e \sim 2000$ larger than for the canonical CR-I.

When leptons with large Lorentz factors are involved, it is worth checking the condition that the NRSI growth rate is larger than the synchrotron loss rate (Rybicki & Lightman 1986). Losses are negligible[5] as long as the electron Lorentz factor γ_e satisfies:

$$\gamma_e \ll 3.7 \times 10^{12}\,\frac{n_{\rm cr}}{n_0}\frac{v_d}{v_{A0}}\left(\frac{B_0}{G}\right)^{-1}. \quad (10)$$

In astrophysical environments, e.g., for shocks in the interstellar medium, one has $n_{\rm cr}/n_0 \sim 10^{-7}$, and $B_0 \sim 3\,\mu$G, $v_d/v_{A0} \sim 10$, for which Equation (10) returns an upper limit of $\gamma_e \sim 10^{12}$, i.e., the effect of synchrotron losses are negligible. However, in laboratory experiments the above condition must be reckoned with, since $B_0 \sim 10^3$ G, n_0 is large, which are needed for satisfying $\gamma_{\rm fast} < \omega_{\rm ci}$ (Jao et al. 2019).

Combining Equations (8) and (9), and the condition $\gamma_{\rm fast} < \omega_{\rm ci}$, we find that the necessary momentum to drive the NRSI by an arbitrary mass of CRs is

$$p_{\rm cr} \gg m_i v_{A0}\frac{\omega_{\rm ci}}{\gamma_{\rm fast}}. \quad (11)$$

In the following sections we test these expectations with self-consistent kinetic simulations using CR beams with species of different mass and charges.

[5] Technically, for large values of ξ, when $\delta B \gg B_0$ is expected, losses may affect the NRSI saturation for smaller values of γ_e.

3. Numerical Setup

We perform simulations using the massively parallel electromagnetic PIC code *Tristan-MP* (Spitkovsky 2005). We consider Cartesian geometry, including all three components of the particle velocities and of the electromagnetic fields. The parameters used in our simulations are listed in Table 1 and outlined below.

3.1. Simulation Box and Magnetic Field

Most of the simulations are performed in a quasi-1D geometry, with five cells along y and N_x cells along x; the physical length of the box is chosen to be at least $\approx 6\,\lambda_{\rm fast}$ to ensure that the domain spans several wavelengths of the fastest-growing mode. We use five cells per d_e and a time step is set by the speed of light and grid space, such that $\Delta t = 0.04\,\omega_{\rm pe}^{-1}$; we checked the convergence of our results with such resolutions.

Simulations are initialized with a uniform magnetic field along the x direction, whose strength is parameterized via the magnetization $\sigma \equiv (\omega_{\rm ce}/\omega_{\rm p})^2$, where $\omega_{\rm p} = \omega_{\rm pe}(1 + m_e/m_i)^{1/2}$; for our benchmark runs we set $\sigma = 10^{-2}$, which corresponds to an Alfvén speed of $v_{A0}/c = (\sigma m_e/m_i)^{1/2} = 10^{-2}$.

Although $B_{\rm y,z} = 0$ at $t = 0$, the thermal motion of the plasma electrons and ions develops a nonzero $B_\perp$ after a few time steps, which acts as a seed field for the instability. The seed field can be reduced by initializing a smaller plasma temperature at $t = 0$; however, we have checked that the final result is unaffected by this choice for relatively cold plasmas (see, e.g., Reville et al. 2008; Zweibel & Everett 2010, for warm-plasma corrections).

3.2. Background Plasma

Each computational cell is initialized with 50 macroparticles, half representing ions and half electrons. An artificial ion to electron mass ratio, $m_i/m_e = 100$, is used to keep the simulations computationally tractable. Both ion and electron distributions are initialized as Maxwellians with temperature $T_i = T_e = 6.4 \times 10^{-3}\, m_e c^2/k_B$, where k_B is the Boltzmann constant.

3.3. CRs

To be in the NRSI regime, $n_{\rm cr} \ll n_0$ is needed so, to boost the CR counting statistics, we use 25 CR particles per cell with weights tuned to set the ratio $n_{\rm cr}/n_0$ as described in Table 1 (see, e.g., Riquelme & Spitkovsky 2009); to retain the quasi-neutrality, the weights of the background electrons are either increased or decreased depending on the sign of the CRs. This means that in the CR-I (CR-E) case, the thermal plasma contains a slightly larger number of electrons (ions). For all three species (ion, electrons, and CRs), the initial spatial distribution of macroparticles in a computational cell is the same, which ensures a zero electric field at $t = 0$.

In the reference frame in which CR are isotropic, they have momentum $p'_{\rm cr} = \gamma_{\rm cr} m_{\rm cr} v'_{\rm cr}$ (where $v'_{\rm cr}$ is the isotopic velocity; assuming a mono-energetic CR distribution); for a meaningful comparison between the CR-I and CR-E cases, we use the same CR momentum for both species (see Equation (9)).

The isotropic CR distribution is boosted with velocity $v_{\rm bst}$ with respect to the background thermal ions, which are initially at rest; thermal electrons have a drift velocity defined by Equation (1). Due to the Lorentz transformation, the effective drift velocity between CRs and thermal plasma along the x-axis

Table 1
Simulation Parameters for Different Runs

Run	N_x	N_y	$\frac{d_e}{\Delta_x}$	$\frac{m_i}{m_e}$	$\frac{v_{A0}}{c}$ $\times 10^{-2}$	$\frac{v_{bst}}{c}$	$\frac{n_{cr}}{n_0}$ $\times 10^{-3}$	$\frac{p'_{cr}}{m_i c}$	$\frac{v_d}{c}$	ξ	$\frac{k_{fast}}{1/d_e}$ $\times 10^{-2}$	$\frac{\gamma_{fast}}{\omega_{pe}}$ $\times 10^{-4}$
A. EI-S-ξ340 ★	3×10^4	5	5	100	1	0.8	4	10	0.635	340	1.27	1.27
B. EI-S-ξ56	3×10^4	5	5	100	1	0.8	4	1	0.740	56	1.48	1.48
C. EI-S-ξ53	5×10^4	5	5	100	4	0.8	10	10	0.635	53	0.79	3.2
D. EI-S-ξ11	10×10^4	5	5	100	1	0.2	4	10	0.135	11	0.27	0.27
E. EI-M-ξ170	3×10^4	5	5	100	1	0.8	6, 4	10, 10	0.635	170	0.635	0.635
F. EI-M-ξ68	6×10^4	5	5	100	1	0.8	4.8, 4	10, 10	0.635	68	0.254	0.254
G. EI-M-ξ0	500	500	5	100	1	0.8	4, 4	10, 10	0.635	0	…	…
H. EP-S-ξ42	3×10^4	5	5	1	1	0.8	1	10	0.635	42	2.25	1.59
I. EP-M-ξ0	4000	250	5	1	0.32	0.8	1, 1	10, 10	0.635	0	…	…

Note. Columns indicate the number of cells along the x and y directions, number of cells per electron skin depth, mass ratio, Alfvén speed, boost speed, CR density and momentum in their rest frame, effective drift speed (see Equation (12)), and parameter ξ (Equation (9); for estimating the value of ξ, see the example given after Equation (13)), and the expected k-mode and growth rate for the most unstable mode (Equations (7) and (8)). The nomenclature "EI-S-ξ53" represents a run where the background is made of electron-ion (EI) plasma, CR beam contains a single (S) charged species, and $\xi \approx 53$. Runs E–G: CRs contain a mixed (M) population of positive and negative charges where $m_i\gamma_i = m_e\gamma_e = 10$ (pair beam in an EI plasma). Runs H and I are similar to the previous case, except that here $m_i = m_e$ (pair beam in pair plasma). The symbol "★" marks the benchmark simulation.

becomes

$$v_d = \frac{1}{2}\int_{-1}^{1} d\mu \frac{\mu\, v'_{cr} + v_{bst}}{1 + \mu\, v'_{cr}\, v_{bst}/c^2}. \quad (12)$$

Note that the boost velocity is not identical to the drift velocity. When comparing with the analytic predictions, we use the drift velocity, which depends on the boost speed and the CR distribution. In the simulation frame, the average momentum per particle is also modified to

$$p_{cr,x} = \frac{1}{2}\int_{-1}^{1} d\mu \frac{\mu\, p'_{cr} + E'_{cr}\, v_{bst}/c^2}{[1 - (v_{bst}/c)^2]^{1/2}} = \gamma_{bst}\, v_{bst}\frac{E'_{cr}}{c^2}, \quad (13)$$

where $E'_{cr} = \gamma_{cr} m_{cr} c^2$, $\gamma_{bst} = 1/[1 - (v_{bst}/c)^2]^{1/2}$. For our fiducial parameters: $v_{bst} = 0.8c$, $|p'_{cr}| = 10\, m_i\, c$, we find $v_d \simeq 0.635c$ and $p_{cr,x} \simeq 13.4\, m_i\, c$, which yield $\xi \approx 340$ (Equation (9)). For $t > 0$, all species are allowed to evolve self-consistently under periodic boundary conditions.

4. Results

4.1. Maximally Unstable Modes

The magnetic field profiles for our benchmark parameters (Run A in Table 1) are shown in Figure 3, which are taken at $t \simeq 7.4\, \gamma_{fast}^{-1}$; where both times and lengths are normalized to the prediction for the fastest-growing mode (γ_{fast}^{-1} and $\lambda_{fast} \equiv 2\pi/k_{fast}$, see Equations (7) and (8)). Black, red, and blue lines correspond to the x, y, and z components of $\boldsymbol{B}$ normalized to B_0. While B_x cannot[6] change in a quasi-1D setup, the perpendicular components show a dominant mode with a wavelength of $\approx\lambda_{fast}$ consistent with Equation (7). Comparing the CR-I and CR-E driven runs (top and bottom panels of Figure 3, respectively), we see that the magnitude and wavelength of the dominant mode are very similar. However, in the top panel, B_z (blue) leads B_y (red), while in the bottom panel it trails B_y; this is associated with the helicity of the growing modes, consistent with Equation (5).

[6] This is also due to the use of smoothing filters in the PIC simulations to reduce the numerical noise in the current density, which finally goes into the Ampère–Maxwell equation and produces almost identical fields along the y-axis in our quasi-1D setup.

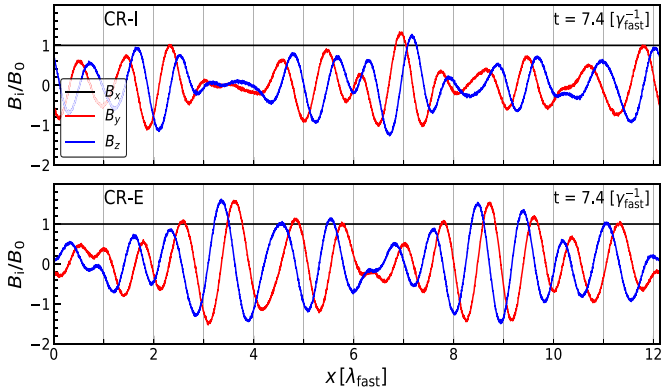

Figure 3. Snapshot of the magnetic field component at $t \simeq 7.4\, \gamma_{fast}^{-1}$ as a function of x, in units of $\lambda_{fast} \simeq 494.7\, d_e$, for the benchmark run A. EI-S-ξ340 (Table 1). Top and bottom panels display the CR-I and CR-E cases, respectively. For both cases, a typical mode of wavelength $\approx\lambda_{fast}$ is evident.

The helicity of each mode with wavenumber k can be formally expressed by the phase difference of the perpendicular magnetic fields, $\Delta\phi(k)$ (Equation (5)), written as a function of the Stokes parameters (Q, U, V; see Equation (A14) in Appendix A):

$$\Delta\phi(k) = -\tan^{-1}\left[\frac{V(k)}{(Q^2(k) + U^2(k))^{1/2}}\right], \quad (14)$$

For a given k, the helicity depends on the sign of $\Delta\phi$; a mode is RH if $\Delta\phi(k) > 0$ and LH if $\Delta\phi < 0$ and the polarization is exactly circular if $|\Delta\phi| = \pi/2$.

The phase difference $\Delta\phi(k)$ is shown in Figure 4 as a function of time for the CR-I (upper panel) and CR-E (lower panel) cases. For $k \lesssim k_u$ (left of the vertical dotted line), we have that $\Delta\phi \to \pm\pi/2$ for the CR-I and CR-E cases, consistent with expectations of the RH and LH modes, respectively. For $k > k_u$, modes do not have a fixed mode of polarization, in that both branches have a comparable amplitude and do not grow in the linear stage compared to other modes (see Section 4.2).

By looking at the time evolution of $\Delta\phi$ (vertical axis in Figure 4), we find that after $t \approx 9\gamma_{fast}^{-1}$, the red/blue regions deviate from the linear prediction (vertical dashed–dotted line).

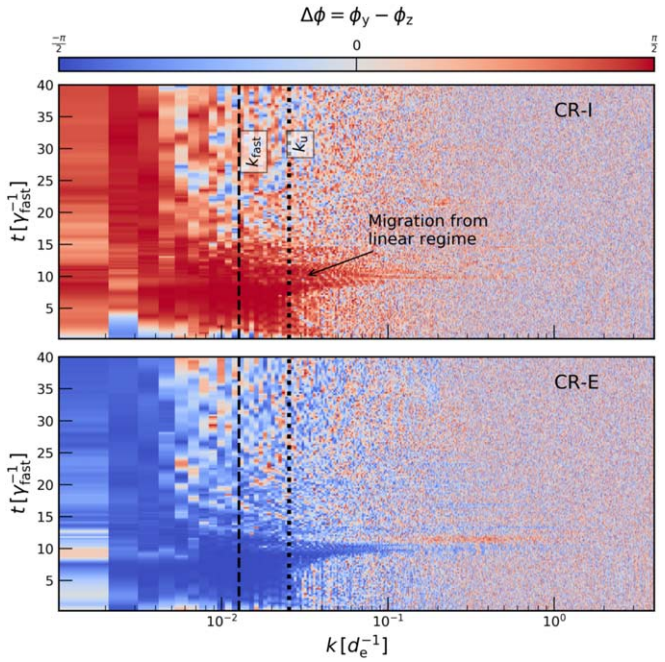

Figure 4. Time evolution of the phase difference $\Delta\phi$ (a proxy for helicity, see Equation (14)) for our benchmark run. Top and bottom panels display the CR-I and CR-E cases. The two vertical lines, dashed and dotted, denote $k_{\rm fast} = 1.27 \times 10^{-2}\, d_e^{-1}$ and $k_u = 2k_{\rm fast}$. For $k > k_u$ (Regime I in Figure 2) waves do not have a fixed helicity, whereas for $k < k_u$ (Regime II), $\Delta\phi$ is either $\approx +\pi/2$ or $-\pi/2$, corresponding to the RH (CR-I case) or LH (CR-E case) modes. Deviation from the linear theory is observed for $t \gtrsim 10\,\gamma_{\rm fast}^{-1}$.

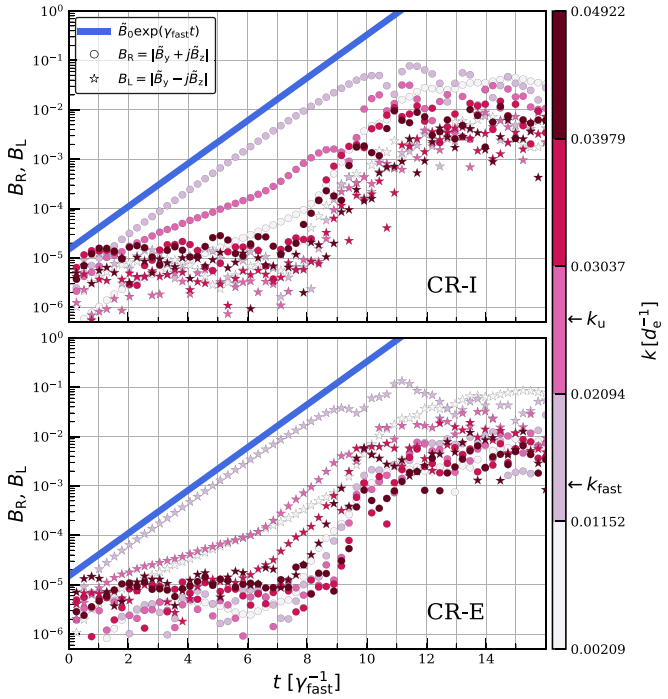

Figure 5. Time evolution of the LH (B_L, stars) and RH (B_R, circles) modes for five different wavenumbers k. In the CR-I case, the RH modes grow the fastest, whereas in the CR-E case the magnetic field is dominated by growing LH modes. In both cases, the value of k for the fastest-growing mode is $\approx 0.0127\, d_e^{-1}$ (lilac). The simulation shows a good agreement with the analytic prediction for $k = k_{\rm fast}$ (blue solid line) until $t \approx 9\,\gamma_{\rm fast}^{-1}$, after which the evolution becomes nonlinear. Note that when $t \gtrsim 12\,\gamma_{\rm fast}^{-1}$, the amplitude of the fastest-growing mode becomes subdominant and longer wavelength modes take over.

This is due to the CR backreaction: the thermal plasma is set in motion (see, e.g., Equation (A16) in Appendix A.2) and v_d is reduced, and modifies the upper limit, k_u. At $t \approx 9\gamma_{\rm fast}^{-1}$, the resonant branch also starts to grow very rapidly (Figure 5) and the helicity is no longer sharp. When $t \gtrsim 12\gamma_{\rm fast}^{-1}$, the system becomes nonlinear.

4.2. Growth Rate

To compare the growth rate in the CR-I and CR-E cases, in Figure 5 we show the time evolution of the RH and LH modes ($B_{\rm R} \equiv \tilde{B}_y + j\tilde{B}_z$, circles, and $B_L \equiv \tilde{B}_y - j\tilde{B}_z$, stars, where $\tilde{B}_{\rm y,z}(k)$ are the Fourier transform of $B_{\rm y,z}(x)$ along the x-axis) for different values of k. Again, we see that in the CR-I case (top panel) RH modes with $k \lesssim k_u = 0.0254 d_e^{-1}$ grow faster than their LH counterparts until $t \approx 9\,\gamma_{\rm fast}^{-1}$; the opposite is true for the CR-E case (bottom panel). A comparison between the blue solid line (showing the expected evolution of the fastest-growing mode) and purple colored circles (upper panel) or stars (lower panel) for $k_{\rm fast} = 0.0127 d_e^{-1}$ indicates that the growth rate of the fastest-growing mode is the same for both cases, consistent with Equation (8). Note that as long as the modes remain quasi-linear ($t \lesssim 9\,\gamma_{\rm fast}^{-1}$), modes with $k > k_u$ (red/brown circles/stars) in the non-unstable branch just oscillate, as suggested in Section 2.2. For $t \gtrsim 9\,\gamma_{\rm fast}^{-1}$, both the RH and LH modes evolve similarly, likely because of a power transfer between modes of different helicities (e.g., Chin & Wentzel 1972), when the system has entered its nonlinear regime (also see Figure 4).

In summary, the CR-E case produces a result similar to that of the CR-I case when γ_e in the CR beam $\approx m_i/m_e\gamma_i$. Next, we use this result to explore NRSI in other environments where the NRSI can be potentially important.

4.3. NRSI in Different Environments

In previous sections, we have presented the cases where the CR populations are comprised entirely of either ions or electrons. However, in some astrophysical environments, energetic particles consist of both energetic positrons and electrons and the thermal background can be a pair plasma. If there is a difference in acceleration efficiency between these two species (e.g., Cerutti et al. 2015; Philippov & Spitkovsky 2018), then they can generate a current, which may drive the NRSI. When such relativistic electrons are liberated into the interstellar medium (an EI plasma), they may excite the NRSI and amplify the magnetic field that may be crucial for the self-confinement of CRs near their sources, as revealed, e.g., by the γ-ray halos detected around PWNe (e.g., Abeysekara et al. 2017).

Denoting the number density of positive and negative charges by n_+ and n_- respectively, the linear theory predicts that the growth of the NRSI depends on the effective CR current density, $J_{\rm cr} \equiv (n_+ - n_-)e\,v_d$, which physically corresponds to the return current in the background plasma. However, since the helicity of waves excited by positrons and electrons are opposite, PIC simulations are necessary to assess the extent to which a pair beam can be viewed as a linear superposition of their opposite currents. To cover different scenarios, we now investigate the NRSI driven by CRs of both charges on top of two different thermal backgrounds: ion-electron (Section 4.3.1) and electron-positron plasmas (Section 4.3.2).

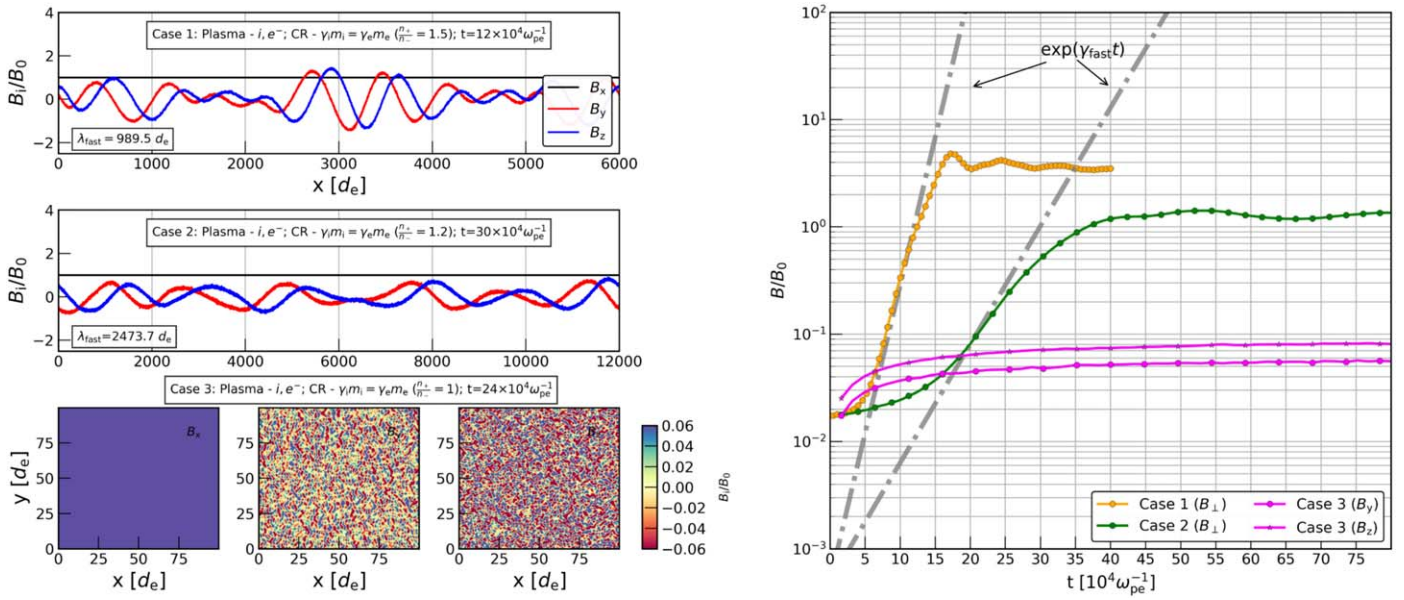

Figure 6. NRSI driven by pair beams in a ion-electron background (Runs E–G in Table 1). Left panels: snapshots of the B field for three cases with different ratio n_+/n_-. Right panel: time evolution of the B field for the corresponding cases; the exponential phase is well described by the linear theory outlined here, except for the zero-current case 3 (Run G).

4.3.1. Pair Beam in an Ion-electron Plasma

We first consider an ion-electron background plasma with $m_i/m_e = 100$ (as in previous sections), and CRs with the Lorentz factors $\gamma_i m_i = \gamma_e m_e = 10$. We allow n_+ and n_- to be different, since positrons and electrons can be accelerated in different regions with different net electric charges. For instance, in the equatorial region of a pulsar magnetosphere the reconnecting current sheet produces more energetic positrons than electrons for an aligned rotator[7] (Cerutti et al. 2015; Philippov & Spitkovsky 2018). Even if the ultimate mechanism responsible for the acceleration of the bulk leptons that shine in a PWNe is still under debate, it is arguable that such magnetospheric particles play a crucial role, likely acting at least as seeds for further acceleration, possibly at the wind termination shock. Therefore, *pair* beams in and around PWNe may be either neutral or present an excess of particles of one sign.

Let us first consider the regime $n_+ > n_-$, and more precisely, two cases in which there are 50% and 20% more positively charged particles (labeled by case 1 and case 2 in Figure 6, respectively; the corresponding parameters are detailed in runs E and F of Table 1). The snapshots of the B field for these two cases are shown in the top- and middle-left panels of Figure 6. We find that the wavelength and growth rate of the fastest-growing mode agree well with the linear theory when an effective number density of CRs $n_{cr} = n_+ - n_-$ is used. This is shown by the gray dashed–dotted and dotted lines in the right panel in the same figure, which displays the evolution of B in time for both cases. Note that for lower effective currents (20% excess, green curve) the growth rate is smaller and also the saturation of the NRSI occurs at smaller values, still $B_\perp/B_0 \gtrsim 1$ for our parameters.

The third case considers the scenario $n_+ = n_-$, where we observe that the NRSI is quenched, as expected from the linear theory for a null CR current. This can be seen in the lower-left panels of Figure 6 (Run G in Table 1) and also from the right panel of the same figure (magenta curves). Note that the system still has free energy because of the CR anisotropy, and in fact, we observe evidence of small-scale fluctuations and a marginal amplification of the magnetic field, possibly associated with the gyro-resonant instability discussed by Lebiga et al. (2018).

This situation may be more similar to the case of the relativistic beams of pairs produced by the interaction of blazar teraelectronvolt photons with the extragalactic background light, though in a significantly more magnetized background plasma (the electrostatic oblique instability, see, e.g., Sironi & Giannios 2014; Shalaby et al. 2017, and references therein). A more detailed investigation of this regime is left to a further work, but here we stress that even a relatively small excess of one charge with respect to the other, as naturally expected from pulsars, is likely sufficient to put the system in the Bell (or resonant) regime.

4.3.2. Beams in Pair Plasmas

Let us now consider the development of the NRSI in a pair plasma (runs H and I in Table 1). At first we investigate the effect of a background pair plasma on the standard NRSI; we take the current to be made of only positively charged particles, i.e., positrons, and therefore expect results similar to the CR-E cases. While estimating the growth rate, one has to recall that posing $m_i = m_e$ reduces k_{fast} and γ_{fast} by a factor of $2^{1/2}$ and 2 compared to the standard ($m_i \gg m_e$) prediction (Equations (7) and (8), respectively). These factors are due to the fact that v_{A0} in Equation (7) is practically $v_{A0i} = v_{A0}(1 + m_e/m_i)^{1/2}$, and $\mathcal{A}$ in Equation (A13) is 2 instead of 1 (for details, see Appendix A). The simulations that we performed in this regime confirm such theoretical estimates and easily produce $B_\perp/B_0 \gtrsim 1$ as expected, so we do not show them here.

For a pair background, it is possible to envision a scenario (e.g., in relativistic shocks, see Sironi & Spitkovsky 2009), in which both electrons and positrons are accelerated in the same way and the effective current in CRs is zero. This case (Run I in Table 1) is illustrated in Figure 7, which displays the three components of the magnetic field (left panels) and their time evolution (right panel).

[7] The opposite would be true for an anti-aligned rotator, where the angle between magnetic and rotation axes is $\sim\pi$ instead of 0.

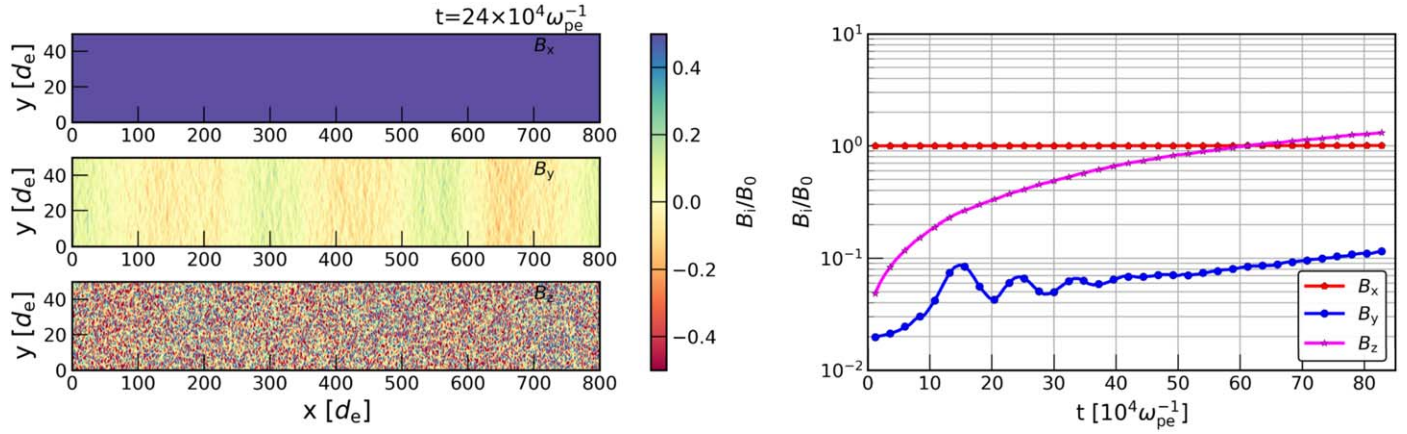

Figure 7. NRSI in pair plasma for a zero beam current case (Run I in Table 1). Left panels: components of B at $t = 24 \times 10^4\,\omega_{\rm pe}^{-1}$, showing filaments of size $\sim d_e$. Right panel: time evolution of corresponding components; the growth of the instability is very different from the standard theory of NRSI.

We point out that there are substantial differences between the EI (Figure 6) and pair (Figure 7) backgrounds. Unlike in the EI case, the out-of-plane component B_z does not saturate at $\delta B \ll B_0$ but grows over the whole simulation; B_y grows at a similar rate, too, but it is smaller by a factor of a few, likely a consequence of the reduced dimensionality of the simulation. This is consistent with the PIC simulations of relativistic shocks in pair plasmas performed by Sironi & Spitkovsky (2009), where electrons and positrons are equally accelerated and produce nonlinear fluctuations in the shock precursor. We also note that, while fluctuations in B_z have very small wavelengths, of the order of the inertial length in both the longitudinal and transverse directions (similar to the case in Figure 6), there is a clear evidence of a long-wavelength longitudinal mode in B_y.

The possibility of developing large-scale (i.e., much larger than d_e) nonlinear fluctuations even for a case with zero-current is indeed intriguing and may have astrophysical implications for the self-confinement of energetic pairs. In any case, this instability is quite different from the NRSI in many aspects, and the anisotropy that we report is likely an artifact of the reduced dimensionality of the presented simulations. A dedicated investigation of this regime with 3D runs is in order but beyond the goals of this paper.

4.4. Saturation

The NRSI is believed to be important for the overall amplification of an initial magnetic field, and the exact mechanism for its saturation is not completely understood. Bell (2004) and Blasi et al. (2015) provided two different heuristic arguments for deriving the expected strength of the amplified magnetic field, which converge in suggesting that at saturation

$$\frac{\delta B^2}{8\pi} \approx \frac{1}{2}\frac{v_d}{c}U_{\rm cr}, \tag{15}$$

where $U_{\rm cr}$ represents the CR energy density. This condition[8] is similar to posing $\xi \approx 1$ in Equation (9), since $P_{\rm cr} \approx v_d U_{\rm cr}/c$, which is also equivalent to stating that when the RSI and the NRSI grow at the same rate, the CR current is disrupted and perturbations cannot grow linearly. On the other hand, kinetic simulations (e.g., Riquelme & Spitkovsky 2009; Gargaté et al. 2010; Caprioli & Spitkovsky 2014; Weidl et al. 2019) have suggested that saturation may be achieved when modes that can scatter the CRs have grown sufficiently, a statement that is hard to quantify in the nonlinear stage; therefore, the question arises as to whether CR-I and CR-E NRSI evolve and saturate in a similar way.

To investigate the saturation of the magnetic field, we explore different plasma and CR parameters such as v_{A0}, $n_{\rm cr}/n_e$, v_d, and $p_{\rm cr}$ (see Table 1) and display the evolution of the transverse magnetic field in Figure 8. All the simulations have $\xi \gg 1$ and in fact are conducive to $B_\perp/B > 1$. By comparing the red and blue curves (representing the CR-I and CR-E cases), we conclude that the time evolution and the saturation of magnetic field amplification depends only on the dynamic mass of CR particles, and not on the charge of the CR current.

Although we have used the mono-energetic CR distribution throughout this work, we expect that different CR distributions will produce similar results because the linear growth depends on the net current density in the CR beam, which is dominated by the CR number density (see, e.g., Haggerty et al. 2019). This is also valid for the power-law CR distribution. In such cases, to compare with our predictions, the effective current, drift velocity, and the anisotropic CR pressure need to be calculated by integrating the CR distribution (see, e.g., Equation (12)). The saturation may slightly depend on the highest energy particles because they have a larger Larmor radius and can be nonresonant ($R_L \gg \lambda_{\rm fast}$) with the amplified modes. Even in this scenario, we expect the saturation to occur within our theoretical prediction, which is based on the momentum conservation as illustrated below.

For a qualitative estimate of the saturated magnetic field in our simulations, we extend our linear analysis by using a semiclassical approach (Appendix A.2), which is compared with simulations and displayed in the right panel of Figure 8. The top of the cyan lines represents the upper limit of the final $B_\perp/B_0$, which matches Equation (15); also see Section 2.3 in Gupta et al. (2021). Note that saturation may be slightly different if CRs were continuously replenished, rather than obeying periodic boundary conditions as in the present setup. Although Figure 8 shows a reasonable agreement with theoretical prediction, we want to draw attention to the cases where the mixed composition of CRs are shown (in particular Run F—green triangle). The saturated $B_\perp/B_0$ for these runs is

[8] For a shock, $\xi \approx \epsilon \mathcal{M}_A^2 (v_d/c)$, where $\mathcal{M}_A$ is the Alfvén Mach number, v_d is the speed of the shock in upstream frame, and $\epsilon = U_{\rm cr}/(\rho v_d^2) \sim 0.1$ is CR acceleration efficiency (e.g., Caprioli & Spitkovsky 2014).

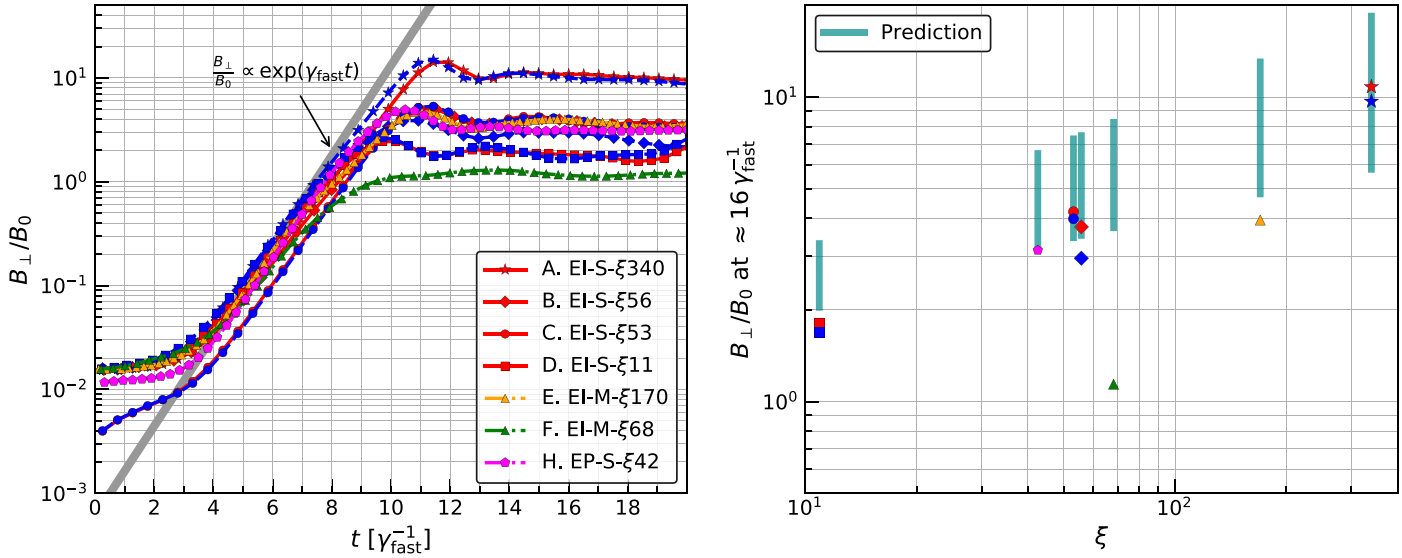

Figure 8. Left panel: time evolution of the box-averaged transverse field $B_\perp/B_0$ for all runs (except the zero beam current runs G and I) listed in Table 1. The gray line shows the expected linear growth. Comparing the gray lines with our simulations, we find that for the CR-E (blue dashed curves) and CR-I (red solid curves) cases, B evolves similarly and saturates at the same level. Right panel: $B_\perp/B_0$ at saturation ($t \sim 16\,\gamma_{\rm fast}^{-1}$) as a function of the ξ parameter, a proxy for NRSI prominence over RSI (see Equation (9) and Table 1). The cyan lines show the expectations from Appendix A.2 (see, e.g., Equation (A21)).

appreciably smaller than the prediction, as mentioned above. This is probably because in the mixed beam compositions, the growing fields can also resonantly interact with beam particles, causing the saturation to occur at a smaller value than that expected from a pure nonresonant calculation. An important result is that the NRSI, whether driven by a mixed CR composition or in a different background plasma, typically results in $B_\perp/B_0 \gtrsim 1$.

5. Summary

We have investigated the NRSI for different charge, mass, and mixed compositions of CRs in different backgrounds. We performed a linear analysis in Section 2 and confirmed the analytic predictions using self-consistent PIC simulations. Our results are summarized in the following.

1. Regardless of the nature of the current-carrying species, the main requirement for driving NRSI, and hence nonlinear field amplification, is that the CR momentum flux must be much larger than the magnetic pressure in the background plasma (Equation (9)).
2. The growth rate in the CR-I and CR-E cases are comparable at a fixed current, but the helicity of the unstable modes is opposite in the CR-I and CR-E-driven cases (Figure 4); this is a consequence of the opposite sign of the return current in thermal electrons that compensates the CR current (Figure 1).
3. A beam encompassing both positive and negative charges can drive the NRSI and lead to nonlinear field amplification, as long as it has a net current, which determines the actual growth rate (Figure 6).
4. For a given CR current made of one species only, the magnetic field at saturation ($\delta B/B_0 > 1$) depends on the initial anisotropic momentum flux, and not on its charge (Figure 8). This point suggests that laboratory experiments, with sufficiently powerful lasers (e.g., Jao et al. 2019), may be able to test the Bell instability even with electron beams.
5. For CR distributions with the same momentum flux, but encompassing different charges, less magnetic field is found at saturation (Figure 6). This is a promising path for explaining the origin of the teraelectronvolt halos detected around PWNe (Abeysekara et al. 2017), which are likely produced by escaping energetic leptons. The extent of such halos is consistent with a suppression of the Galactic diffusion coefficient of a factor of $\sim$100, which may be achieved even with linear field amplification, $\delta B/B_0 \lesssim 1$.
6. The NRSI driven by a net current behaves in a similar way in ion-electron and in pair plasmas, which is nontrivial due to the different nature of the return current in the background plasma (Figures 6 and 7). One notable difference is found for the case of a pair beam in a pair plasma, which exhibits more magnetic field amplification than its counterpart in an EI background (Figure 7).

In summary, we have provided a theory/simulation cookbook for the properties of the NRSI (Bell) instability for beams and background made of different species, covering a region of the parameter space that—to our knowledge—had never been tested via kinetic plasma simulations. Applications to given space/astro/laboratory environments will be presented in future works.

We thank the anonymous referee for the valuable suggestions on our manuscript. Simulations were performed on computational resources provided by the University of Chicago Research Computing Center, the NASA High-End Computing Program through the NASA Advanced Supercomputing Division at Ames Research Center, and XSEDE TACC (TG-AST180008). D.C. was partially supported by NASA (grants 80NSSC18K1218, 80NSSC20K1273, and 80NSSC18K1726) and by the NSF (grants AST-1714658, AST-2009326, AST-1909778, PHY-1748958, and PHY-2010240).

Software: Tristan-MP (Spitkovsky 2005).

Appendix A
Details of the Analytic Calculations

At first let us recall the Ampère–Maxwell equation: $\nabla\times \boldsymbol{B} = \frac{4\pi}{c}\boldsymbol{J} + \frac{1}{c}\frac{\partial}{\partial t}\boldsymbol{E}$ and the Maxwell–Faraday equation: $\nabla\times \boldsymbol{E} = -\frac{1}{c}\frac{\partial}{\partial t}\boldsymbol{B}$. In the absence of current source (denoted by $\boldsymbol{J}$), these equations determine propagation of the electromagnetic (EM) waves. Here, we will show that a nonzero $\boldsymbol{J}$ that comes from unbalanced perturbed current in the plasma generates waves can grow/damp/oscillate depending on the modes.

Initially, the bulk speed (v_e) of background electrons (Equation (1)) is such that it balances the CR current, i.e., the total $J = 0$. Suppose plane-wave perturbations are imposed on the background electromagnetic fields, which result in density and velocity fluctuations in the background ions and electrons. Denoting the first-order perturbations with the subscript 1, the total current density at $t > 0$, in the CR + plasma composite system is

$$\begin{aligned}\boldsymbol{J} &= [s_{\rm cr}\, e\, n_{\rm cr}\, \boldsymbol{v}_d] + [e(n_i + n_{1i})\boldsymbol{v}_{1i}] \\ &\quad + [-e(n_e + n_{1e})(\boldsymbol{v}_e + \boldsymbol{v}_{1e})] \\ &= e n_i(\boldsymbol{v}_{1i} - \boldsymbol{v}_{1e}) - e\, n_{1e}\boldsymbol{v}_e - s_{\rm cr}\, e\, n_{\rm cr}\boldsymbol{v}_{1e}. \end{aligned} \tag{A1}$$

Velocity and density perturbations introduced in Equation (A1) are obtained as follows. As the perturbations on the EM field are modulated with $\exp[j(k\,x - \omega\, t)]$ (where $\boldsymbol{k} = k\,\hat{\boldsymbol{x}}$ is the propagation vector and ω is the angular frequency), linearization of the Lorentz force equation (Equation (2)) gives

$$v_{1x\alpha} = \frac{jq_\alpha}{m_\alpha\omega}E_{1x} \tag{A2}$$

$$v_{1y\alpha} = \frac{jq_\alpha}{m_\alpha\omega}\left[\frac{1 - v_0\, k/\omega}{1 - (\omega_{c\alpha}/\omega)^2}\left(E_{1y} + j\frac{\omega_{c\alpha}}{\omega}E_{1z}\right)\right] \tag{A3}$$

$$v_{1z\alpha} = \frac{jq_\alpha}{m_\alpha\omega}\left[\frac{1 - v_0\, k/\omega}{1 - (\omega_{c\alpha}/\omega)^2}\left(-j\frac{\omega_{c\alpha}}{\omega}E_{1y} + E_{1z}\right)\right], \tag{A4}$$

where we have used the linearized Maxwell–Faraday equation (given below) to substitute the $\boldsymbol{B}$ field:

$$B_{1y} = -\frac{k\, c}{\omega}E_{1z}, \text{ and } B_{1z} = \frac{k\, c}{\omega}E_{1y} \tag{A5}$$

In Equations (A3) and (A4), $\omega_{c\alpha} = q_\alpha B_0/m_\alpha c$ is the cyclotron frequency and $v_0 = s_{\rm cr}v_e \neq 0$ only for electrons ($v_e = |\boldsymbol{v}_e$; Equation (1)). The density fluctuations can be obtained from the ion and electron mass continuity equations, which give $n_{1i} = n_i k\, v_{1{\rm xi}}/\omega$ and $n_{1e} = n_e k\, v_{1{\rm xe}}/(\omega - k\, v_e s_{\rm cr})$, respectively. Substituting Equations (A2)–(A4) in Equation (A1) and neglecting higher order terms of $\omega/\omega_{\rm ci}$ and $\omega/\omega_{\rm ce}$ (as our regime of interest $\omega \ll \omega_{\rm ci}$), we obtain

$$J_{1x} = \frac{j\, E_{1x}}{4\pi\omega}\left[\omega_{\rm pi}^2 + \omega_{\rm pe}^2\left(1 + \frac{s_{\rm cr}v_e k}{\omega - s_{\rm cr}v_e k} + s_{\rm cr}\frac{n_{\rm cr}}{n_i}\right)\right], \tag{A6}$$

$$\begin{aligned}J_{1y} = -\frac{j\, c\, \omega_{\rm pi}}{4\pi v_{A0}}\Bigg[&E_{1y}\left\{\frac{\omega}{\omega_{\rm ci}} + \left(\frac{\omega}{\omega_{\rm ce}} - s_{\rm cr}\frac{v_e k}{\omega_{\rm ce}}\right)\right. \\ &\left.\left(1 + s_{\rm cr}\frac{n_{\rm cr}}{n_i}\right)\right\} + j\, E_{1z}\left\{s_{\rm cr}\frac{v_e k}{\omega}\left(1 + s_{\rm cr}\frac{n_{\rm cr}}{n_i}\right) - s_{\rm cr}\frac{n_{\rm cr}}{n_i}\right\}\Bigg],\end{aligned} \tag{A7}$$

$$\begin{aligned}J_{1z} = -\frac{j\, c\, \omega_{\rm pi}}{4\pi v_{A0}}\Bigg[&-j\, E_{1y}\left\{s_{\rm cr}\frac{v_e k}{\omega}\left(1 + s_{\rm cr}\frac{n_{\rm cr}}{n_i}\right) - s_{\rm cr}\frac{n_{\rm cr}}{n_i}\right\} \\ &+ E_{1Z}\left\{\frac{\omega}{\omega_{\rm ci}} + \left(\frac{\omega}{\omega_{\rm ce}} - s_{\rm cr}\frac{v_e k}{\omega_{\rm ce}}\right)\left(1 + s_{\rm cr}\frac{n_{\rm cr}}{n_i}\right)\right\}\Bigg].\end{aligned} \tag{A8}$$

Here, we have taken $B_0/(4\pi\, m_i\, n_0)^{1/2}$ as the Alfvén speed v_{A0} (since $m_i \gg m_e$, we can take $v_{\rm A0i} = v_{A0}(1 + m_e/m_i)^{1/2} \simeq v_{A0}$). $\omega_{\rm ci,e} = |eB_0/m_{\rm i,e}c|$ is the cyclotron frequency, $\omega_{\rm pi,e} = (4\pi\, n_0 e^2/m_{\rm i,e})^{1/2}$ is the plasma frequency for ions/electrons. Equations (A6)–(A8) show that perturbed current density is nonzero, which act as a source in the Ampère–Maxwell equation. Since we assume $n_{\rm cr} \ll n_e$, the transverse components of the current are simplified to $J_{1y}, J_{1z} \approx (\omega^2/k)(-s_{\rm cr}B_{1y}, s_{\rm cr}\, B_{1z})c/(4\pi\, v_{A0}^2)$, indicating a direct dependency on the transverse magnetic fields, i.e., a tiny perturbation in the magnetic field can increase the current, which further amplifies the magnetic field and so on.

A.1. Dispersion Relation

Substituting Equations (A6)–(A8) in the Ampère–Maxwell equation, and combining the Maxwell–Faraday equations:

$$\begin{bmatrix} h_1 & 0 & 0 \\ 0 & h_2 & -j\, h_3 \\ 0 & j\, h_3 & h_2 \end{bmatrix} \cdot \begin{bmatrix} E_{1x} \\ E_{1y} \\ E_{1z} \end{bmatrix} = \begin{bmatrix} 0 \\ 0 \\ 0 \end{bmatrix}, \text{ where} \tag{A9}$$

$$\begin{aligned}h_1 = 1 - \frac{1}{\omega^2}\Bigg[&\omega_{\rm pi}^2 + \omega_{\rm pe}^2 \\ &\times\left(1 + \frac{s_{\rm cr}v_e k}{\omega - s_{\rm cr}v_e k} + s_{\rm cr}\frac{n_{\rm cr}}{n_i}\right)\Bigg],\end{aligned} \tag{A10}$$

$$\begin{aligned}h_2 = k^2 - \frac{\omega^2}{c^2} - \frac{\omega\omega_{\rm pi}}{c\, v_{A0}}\Bigg[&\frac{\omega}{\omega_{\rm ci}} + \left\{\frac{\omega}{\omega_{\rm ce}} - s_{\rm cr}\frac{v_e k}{\omega_{\rm ce}}\right\} \\ &\times\left(1 + s_{\rm cr}\frac{n_{\rm cr}}{n_i}\right)\Bigg], \text{ and} \\ h_3 = \frac{\omega\omega_{\rm pi}}{c\, v_{A0}}&\left[s_{\rm cr}\frac{v_e k}{\omega}\left(1 + s_{\rm cr}\frac{n_{\rm cr}}{n_i}\right) - s_{\rm cr}\frac{n_{\rm cr}}{n_i}\right].\end{aligned} \tag{A11}$$

Equation (A9) gives two distinct solutions:

Solution A: $E_{1\,{\rm y,z}} = 0$. In this case, if $v_e = 0$, then $\omega \approx (\omega_{\rm pi}^2 + \omega_{\rm pe}^2)^{1/2}$, where $\omega_{\rm pi,e} = (4\pi\, n_0 e^2/m_{\rm i,e})^{1/2}$ is the plasma frequency for ions/electrons. This represents plasma oscillations.

Solution B: $h_2 = \pm\, h_3$, we find a quadratic equation of ω: $\omega^2\mathcal{A} - \omega\mathcal{B} - \mathcal{C} = 0$, which provides the dispersion relation in the following form:

$$\omega = \frac{\mathcal{B} + [\mathcal{B}^2 + 4\,\mathcal{A}\,\mathcal{C}]^{1/2}}{2\mathcal{A}}, \text{ where} \tag{A12}$$

$$\mathcal{A} = \left[\left(\frac{v_{A0}}{c}\right)^2 + 1 + \frac{\omega_{ci}}{\omega_{ce}}\left(1 + s_{cr}\frac{n_{cr}}{n_i}\right)\right],$$
$$\mathcal{B} = \omega_{ci}\left[s_{cr}\frac{v_e k}{\omega_{ce}}\left(1 + s_{cr}\frac{n_{cr}}{n_i}\right) \pm s_{cr}\frac{n_{cr}}{n_i}\right],$$
$$\mathcal{C} = k^2\, v_{A0}^2\left[1 \mp s_{cr}\frac{k_u}{k}\left(1 + s_{cr}\frac{n_{cr}}{n_i}\right)\right] \quad \text{(A13)}$$

where we have introduced a parameter $k_u = \omega_{pi}\,|v_e|/c\,v_{A0}$. Using $\omega_{ci} = (v_{A0}/c)\omega_{pi}$, we obtain a simplified expression of $\mathcal{B}$: $\mathcal{B} = v_{A0}\,k_u\left[s_{cr}\frac{k}{k_u}\frac{m_e}{m_i}\frac{v_e}{v_{A0}}\left(1 + s_{cr}\frac{n_{cr}}{n_i}\right) \pm s_{cr}\frac{v_{A0}}{v_d}\right]$, which is simplified to $\mathcal{B} \approx \pm s_{cr}\, v_{A0}^2\, k_u/v_d$. It can be shown that when $v_{A0} \ll v_d$, the term under the square-root in Equation (A12) mostly depends on $4\mathcal{A}\,\mathcal{C}$, i.e., the square-root term can be a complex number depending on the ratio k/k_u. Using these assumptions, Equation (3) is obtained. Note that, if these conditions are not satisfied, then one can still obtain growing modes; however, the wavelength of the fastest-growing mode and the growth rate can deviate from Bell's (2004) prediction, due to contribution of $\mathcal{B}$ to the square-root term of Equation (A12).

Equations (A5) and (A9) suggest that the transverse B field, $\boldsymbol{B}_\perp = B_{1y}\hat{\boldsymbol{y}} + B_{1z}\hat{\boldsymbol{z}} \propto [\hat{y}\exp(\pm j\pi/2) + \hat{z}]$, i.e., $\Delta\phi = \pm\pi/2$ (Equation (5)). To find the phase difference between B_y and B_z for a given mode, k, from our simulation, we have used Equation (14), where

$$Q(k) = [\tilde{B}_y(k)\tilde{B}_y^*(k) - \tilde{B}_z(k)\tilde{B}_z^*(k)],$$
$$U(k) = [\tilde{B}_y(k)\tilde{B}_z^*(k) + \tilde{B}_y^*(k)\tilde{B}_z(k)],$$
$$V(k) = j[\tilde{B}_y(k)\tilde{B}_z^*(k) - \tilde{B}_y^*(k)\tilde{B}_z(k)] \quad \text{(A14)}$$

Here, $\tilde{B}_{y,z}(k)$ are the Fourier transform of $B_{y,z}(x)$ along the x-axis (the superscript "$*$" denotes the complex conjugate).

A.2. Backreaction and Saturation

The above derivation does not include the backreaction from the plasma caused by the growing waves. In later times ($t \gg \gamma_{fast}^{-1}$), the force due to the term, e.g., $\boldsymbol{J}\times\boldsymbol{B}/c$, can affect the momentum of the CRs and plasma. The unstable waves cannot grow for an indefinite amount of time and saturate. Below, we extend our linear analysis to predict the saturation, which is based on the fundamental fact that the net momentum deposited by CRs goes into thermal background through the amplified EM fields. Note that the saturation is a nonlinear process and numerical simulation can provide a better result and therefore our prediction should be treated as an approximated solution.

Let us recall a more general form of the momentum equation of the plasma:

$$\frac{\partial}{\partial t}[n_0(m_i\boldsymbol{v}_i + m_e\boldsymbol{v}_e)] \approx \frac{1}{c}(\boldsymbol{J}\times\boldsymbol{B}) - \nabla(P_i + P_e). \quad \text{(A15)}$$

Here, $P_{i,e}$ is ion-electron pressure in the plasma. We shall take into account two terms in the right-hand side (RHS) of Equation (A15) one by one as done to obtain an approximated solution. First assuming that the second term in the RHS is much smaller than the first term, we obtain the velocity of plasma ions/electrons:

$$v_{1xi,e} \approx \frac{v_{A0}^2}{v_d}\left(\frac{B_\perp}{B_0}\right)^2, \text{ and } v_{1y/zi,e} \approx v_{A0}\left(\frac{B_\perp}{B_0}\right). \quad \text{(A16)}$$

Since we start with $v_{A0} \ll v_d$, $B_\perp = 0$, $v_{1xi,e} \to 0$. With time, the growing $B_\perp$ results in plasma acceleration. Therefore, the plasma ions that were initially treated stationary with respect to the lab frame also start drifting along the x direction. Whereas the equal raise in transverse velocity components mainly contributes to increasing the velocity dispersion of the plasma, and raises the plasma temperature. Assuming the initial thermal energy per particle in the plasma $\approx m\,a_0^2/2 \sim k_B T_0/2$ (T_0 as the initial temperature), the final temperature of the plasma is expected to be

$$T \sim T_0\left[1 + \left(\frac{v_{A0}}{a_0}\right)^2\left(\frac{B_\perp}{B_0}\right)^2\right]. \quad \text{(A17)}$$

Therefore, a larger magnetic field amplification implies an intense heating effect. The second term in the RHS of Equation (A15), which represents the loss in momentum due to plasma heating, is calculated by using Equation (A17):

$$\int dt\,\nabla(P_i + P_e)|_x \approx \int dt\,\mathrm{Re}\left[\frac{j\,k^2}{\omega}\right](n_0\,m_i\,a_i^2\,v_{1xi})$$
$$\approx \int dt\,\frac{k}{v_{A0}}\left[n_0\,m_i\left\{a_{i0}^2 + v_{A0}^2\left(\frac{B_\perp}{B_0}\right)^2\right\}\frac{v_{A0}^2}{v_d}\left(\frac{B_\perp}{B_0}\right)^2\right]. \quad \text{(A18)}$$

Now considering that the net momentum deposited by CRs goes into thermal background, the time integration of the x component of Equation (A15) yields

$$[n_{cr}p_{cr,x}]|_{t=0}^{t} \approx -n_0\,m_i\frac{v_{A0}^2}{v_d}\left(\frac{B_\perp}{B_0}\right)^2 - \int dt\,\nabla(P_i + P_e)|_x. \quad \text{(A19)}$$

LHS: At $t = 0$, $n_{cr}p_{cr,x} = n_{cr}(\gamma_{bst}\,v_{bst}\,E'_{cr}/c^2)$ (Equation (13)). We further assume that in the final stage, the drift velocity of CRs $\tilde{v}_d \approx v_A$ (as observed in the simulation; see, e.g., figure 3 in Gupta et al. (2021)). This gives $\tilde{v}_{bst} \approx v_A$ and $\tilde{\gamma}_{bst} \simeq 1$, i.e., $n_{cr}p_{cr,x} \approx n_{cr}(v_A\,E'_{cr}/c^2)$. We finally obtain

$$\mathcal{P}\left(\frac{B_\perp}{B_0}\right)^4 + \mathcal{Q}\left(\frac{B_\perp}{B_0}\right)^2 + \mathcal{R}\left(\frac{B_\perp}{B_0}\right) - \mathcal{S} = 0, \quad \text{(A20)}$$

where $\mathcal{P} = 1$, $\mathcal{Q} = [2(a_{i0}/v_{A0})^2 + 4]$, $\mathcal{R} = \left[4\frac{n_{cr}}{n_0}\frac{E'_{cr}}{m_i c^2}\frac{v_d}{v_{A0}}\right]$ and $\mathcal{S} = \left[4\frac{n_{cr}}{n_0}\frac{\gamma_{bst}v_{bst}E'_{cr}/c^2}{m_i c}\frac{v_d\,c}{v_{A0}^2}\right]$. The above equation can be solve

numerically and the approximated solution is

$$\frac{B_\perp}{B_0} \approx [(b^2 + 4\xi)^{1/2} - b]^{1/2},$$

$$\text{where } b = 2 + \left(\frac{a_{i0}}{v_{A0}}\right)^2 \text{ and}$$

$$\xi = \left[\frac{n_{\rm cr}}{n_0}\frac{\gamma_{\rm bst} v_{\rm bst} E'_{\rm cr}/c^2}{m_i c}\frac{v_d\, c}{v_{A0}^2}\right]^{1/2}. \quad \text{(A21)}$$

If we neglect the heating losses and take $a_{i0} \ll v_A$ (i.e., the term $\mathcal{P}$ is absent and $\mathcal{Q} \to 4$: cold plasma), then Equation (A20) gives $B_\perp/B_0 \approx (\mathcal{S}/\mathcal{Q})^{1/2} = \xi^{1/2}$, which is identical to Equation (15). These two possible solutions of $B_\perp/B_0$ are referred as the lower and upper limits of $B_\perp/B_0$ and are shown by the cyan lines in Figure 8.

Appendix B
How Large ξ Should be Chosen

A general assumption in the NRSI is that $\xi \gg 1$ (Equation (9)). Here, we explore how large the value of ξ must be chosen to apply the standard theory of NRSI safely. From Section 2, we recall that the growing modes in the CR-E case have negative helicity. Following the results presented in Section 4.1, we check how $\Delta\phi(k)$ changes as a function of ξ by altering v_{A0} and $n_{\rm cr}$ (other parameters similar to Run B in Table 1). Figure 9 indicates that the dominating modes have $\Delta\phi \approx -\pi/2$ (blue regions) when $\xi \gtrsim 4$, i.e., below $\xi \approx 4$, the NRSI and the RSI blend into each other.

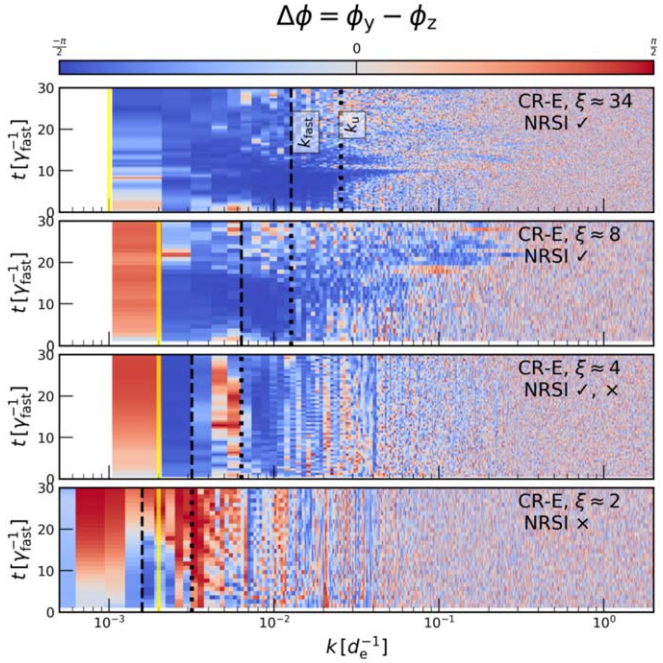

Figure 9. Phase difference $\Delta\phi$ for different modes as a function of time with descending ξ (upper to lower panels). The yellow lines show $k = 1/R_L$. For the upper two panels, the results are consistent with linear theory. For a smaller ξ, the NRSI becomes subdominant and the linear theory outlined here is not applicable.

ORCID iDs

Siddhartha Gupta https://orcid.org/0000-0002-1030-8012
Damiano Caprioli https://orcid.org/0000-0003-0939-8775
Colby C. Haggerty https://orcid.org/0000-0002-2160-7288

References

Abeysekara, A. U., Albert, A., Alfaro, R., et al. 2017, Sci, 358, 911
Achterberg, A. 1983, A&A, 119, 274
Amato, E., & Blasi, P. 2009, MNRAS, 392, 1591
Bell, A. R. 2004, MNRAS, 353, 550
Bell, A. R., & Lucek, S. G. 2001, MNRAS, 321, 433
Berezhko, E. G., & Völk, H. J. 2004, A&A, 427, 525
Blasi, P., Amato, E., & D'Angelo, M. 2015, PhRvL, 115, 121101
Bohdan, A., Niemiec, J., Pohl, M., et al. 2019, ApJ, 878, 5
Bret, A. 2009, ApJ, 699, 990
Bret, A., Gremillet, L., & Dieckmann, M. E. 2010, PhPl, 17, 120501
Bykov, A. M., Brandenburg, A., Malkov, M. A., & Osipov, S. M. 2013, SSRv, 178, 201
Caprioli, D., Haggerty, C. C., & Blasi, P. 2020, ApJ, 905, 2
Caprioli, D., Pop, A., & Spitkovsky, A. 2015, ApJL, 798, 28
Caprioli, D., & Spitkovsky, A. 2014, ApJ, 794, 46
Cerutti, B., Philippov, A., Parfrey, K., & Spitkovsky, A. 2015, MNRAS, 448, 606
Chin, Y.-C., & Wentzel, D. G. 1972, Ap&SS, 16, 465
Choudhuri, A. R. 1998, The Physics of Fluids and Plasmas: An Introduction for Astrophysicists (New York: Cambridge Univ. Press)
Gargaté, L., Fonseca, R. A., Niemiec, J., et al. 2010, ApJL, 711, L127
Guo, X., Sironi, L., & Narayan, R. 2014a, ApJ, 794, 153
Guo, X., Sironi, L., & Narayan, R. 2014b, ApJ, 797, 47
Gupta, S., Caprioli, D., & Haggerty, C. 2021, arXiv:2110.12426
Haggerty, C., Caprioli, D., & Zweibel, E. 2019, ICRC, 36, 279
Haggerty, C. C., & Caprioli, D. 2020, ApJ, 905, 1
Halekas, J. S., Whittlesey, P., Larson, D. E., et al. 2020, ApJS, 246, 22
Jao, C.-S., Vafin, S., Chen, Y., et al. 2019, arXiv:1910.13756
Kasper, J. C., Bale, S. D., Belcher, J. W., et al. 2019, Natur, 576, 228
Krall, N., & Trivelpiece, A. 1973, Int. Series in Pure and Applied Physics (Tokyo: McGraw-Hill Kogakusha)
Lebiga, O., Santos-Lima, R., & Yan, H. 2018, MNRAS, 476, 2779
Malaspina, D. M., Halekas, J., Berčič, L., et al. 2020, ApJS, 246, 21
Marret, A., Ciardi, A., Smets, R., & Fuchs, J. 2021, MNRAS, 500, 2302
Masters, A., Stawarz, L., Fujimoto, M., et al. 2013, NatPh, 9, 164
Masters, A., Sulaiman, A. H., Stawarz, Ł., et al. 2017, ApJ, 843, 147
Matthews, J. H., Bell, A. R., Blundell, K. M., & Araudo, A. T. 2017, MNRAS, 469, 1849
Morlino, G., & Caprioli, D. 2012, A&A, 538, A81
Niemiec, J., Pohl, M., Stroman, T., & Nishikawa, K.-I. 2008, ApJ, 684, 1174
Peterson, J. R., Glenzer, S., & Fiuza, F. 2021, PhRvL, 126, 215101
Philippov, A. A. 2017, PhD thesis, Princeton Univ.
Philippov, A. A., & Spitkovsky, A. 2018, ApJ, 855, 94
Reville, B., & Bell, A. R. 2013, MNRAS, 430, 2873
Reville, B., Kirk, J. G., Duffy, P., & O'Sullivan, S. 2008, IJMPD, 17, 1795
Riquelme, M. A., & Spitkovsky, A. 2009, ApJ, 694, 626
Rybicki, G. B., & Lightman, A. P. 1986, Radiative Processes in Astrophysics (Cambridge: Cambridge Univ. Press)
Schroer, B., Pezzi, O., Caprioli, D., Haggerty, C., & Blasi, P. 2021, ApJL, 914, L13
Shalaby, M., Broderick, A. E., Chang, P., et al. 2017, ApJ, 841, 52
Shapiro, V. D., Quest, K. B., & Okolicsanyi, M. 1998, GeoRL, 25, 845
Sironi, L., & Giannios, D. 2014, ApJ, 787, 49
Sironi, L., & Spitkovsky, A. 2009, ApJ, 698, 1523
Spitkovsky, A. 2005, in AIP Conf. Ser. 801, Astrophysical Sources of High Energy Particles and Radiation, ed. T. Bulik, B. Rudak, & G. Madejski (Melville, NY: AIP), 345
Weibel, E. S. 1959, PhRvL, 2, 83
Weidl, M. S., Winske, D., & Niemann, C. 2019, ApJ, 872, 48
Wilson, L. B., Sibeck, D. G., Turner, D. L., et al. 2016, PhRvL, 117, 215101
Winske, D., & Leroy, M. M. 1984, JGR, 89, 2673
Xu, R., Spitkovsky, A., & Caprioli, D. 2020, ApJL, 897, L41
Zacharegkas, G., Caprioli, D., & Haggerty, C. 2019, ICRC, 36, 483
Zirakashvili, V. N., & Ptuskin, V. S. 2008, ApJ, 678, 939
Zweibel, E. G. 1979, in AIP Conf. Ser. 56, Particle Acceleration Mechanisms in Astrophysics, ed. J. Arons, C McKee, & C. Max (Melville, NY: AIP), 319
Zweibel, E. G. 2013, PhPl, 20, 055501
Zweibel, E. G., & Everett, J. E. 2010, ApJ, 709, 1412